University of Baghdad
College of Engineering
JE
JOURNAL OF ENGINEERING

Journal of Engineering

journal homepage: www.jcoeng.edu.iq

Volume 32 Number 9 September 2026

Experimental Evaluation of Water Dropwise Evaporation in a Solar Humidifier using Flat and Dimpled Absorbers

Saad Mohsin Alsaady, **Karima E. Amori** *

Department of Mechanical Engineering, College of Engineering, University of Baghdad, Baghdad, Iraq

ABSTRACT

This work focuses on developing a Low-cost, low-grade electrical-thermal solar humidification system, as a promising solution for freshwater production. To increase the air humidity ratio at the humidifier exit, a designed and instrumented solar humidifier harnesses solar radiation and receives both a forced hot air stream from a solar air collector and water droplets falling onto its absorber plate, where the droplets evaporate. The solar humidifier dimensions were 330 × 50 × 1000 mm. PV panels supplied electrical power to circulate water and air for preheating by a flat-plate and an air solar collector. Key factors influencing air's relative humidity (RH) are air flow rates (0.5 m^3/min to 1.5 m^3/min), water drip rate (4 to 10 drops/s), and the solar humidifier's absorber surface geometry (flat or dimpled). Tests were extended from 8:00 to 17:00 to evaluate air RH and temperature on clear-sky days in Baghdad, Iraq. Results showed that the highest outlet air RH was 61.2%, 72.4%, and 69.9% for water dripping rates of 4, 7, and 10 drops/s, corresponding to 0.167, 0.297, and 0.423 g/s, respectively, with a constant airflow rate of 0.5 m^3/min. The best dripping rate was 7 drops/s. The outlet air RH from the humidifier was 72.4% and 85.6% for flat and dimpled absorbers, respectively, at an airflow rate of 0.5 m^3/min and 7 water drops/s (0.297 g/s). The humidifier's effectiveness was 85% and 70%, respectively. It is concluded that the dimpled absorber achieves significantly better humidification performance than the flat-plate absorber across all airflow rates. The humidifier pressure drops increases from 0.13 Pa to 0.36 Pa for the flat plate and dimpled plate, respectively, at solar noon, for a flow rate of 0.5 m^3/min.

Keywords: Solar humidifier, Dimpled absorber, Solar collector, Evaporation, Droplet.

1. INTRODUCTION

The world consumes energy at a high rate, which, combined with more greenhouse gas emissions, causes environmental problems that worsen climate change indicators and soil pollution **(Wu et al., 2022)**. Water consumption and wastewater production are associated with increased conventional energy use. In line with the green economy, conventional energy use needs to be more efficient, and the transition to renewable energy needs to be

*Corresponding author
Peer review under the responsibility of University of Baghdad.
https://doi.org/10.31026/j.eng.2026.09.11

Article received: 20/05/2026
Article revised: 22/07/2026
Article accepted: 24/07/2026
Article published: 01/09/2026

faster. Renewable energy sources such as solar, wave/tidal, wind, hydroelectric, biofuels, and geothermal can meet up to 25% of society's energy needs by 2030. Solar energy can be utilized for water or space heating, water desalination based on thermal or reverse osmosis RO, hydrogen production, and electricity generation **(Tourab et al., 2023).**

Providing freshwater for humanity by treating saline water or wastewater is a real challenge amid the escalating energy requirements of a growing global population. Conventional desalination technologies, including multi-effect distillation (MED), multi-stage flash (MSF), and reverse osmosis (RO), may not be appropriate solutions for decentralized water production facilities located in remote areas with limited infrastructure and constrained financial resources. Solar-powered humidification–dehumidification (HDH) desalination has attracted considerable attention as a sustainable method for freshwater production. In a conventional HDH system, saline water is evaporated in a humidifier and condensed in a dehumidifier to produce fresh water, with latent heat recovery improving overall efficiency. **(Ali et al., 2024)** employed jute packing in the humidifier that was sprayed with water heated using a conventional solar reflector and received air to evaporate water in the HDH desalination plant. The system achieved a freshwater production of approximately 20 L/day from a collector area of 2 m^2. A predictive model was also developed to evaluate system performance and optimize the desalination process.

Parabolic trough solar collectors are used for water preheating in water basin solar desalination systems with/without nanofluid to optimize thermal performance and productivity **(Tuğan et al., 2025)**. A small-scale economic freshwater system was developed based on a humidification-dehumidification desalination design, utilizing low-temperature heat from renewable sources to meet the growing need for freshwater; these systems can be considered low-capacity systems, producing less than 100 m^3 per day **(Chiranjeevi et al., 2019)**. Many researchers have focused on demonstrating the impact of incorporating locally available materials and porous structures within monoclinic solar stills to enhance thermal storage capacity and extend production periods into nighttime hours **(Lafta and Amori, 2022)**. Innovative solar designs were developed for saline water treatment **(Manesh et al., 2024)**, proposing a solar-wind-powered HDH with an RO system to treat water and produce 5.36 m^3/h of freshwater, with an energy efficiency of 22.09 %. The system also had a relatively short payback period of 6.95 years. Also, the evaporator integrated with advanced materials such as hydrogel **(Li et al., 2026),** porous carbon-based materials **(Zhang et al., 2026)**, and a copper-based solar evaporator **(Wang et al., 2026)** has demonstrated improved potential for seawater or wastewater treatment via interfacial evaporation. Enhancing water interfacial evaporation is achieved by using phase change materials in solar evaporators, as reported by **(Abdelaziz et al., 2026).** They compared the outdoor yield of a hybrid HDH-pyramid solar still with and without waste engine oil using paraffin wax as a heat storage medium and packing material in Suez City, Egypt.

Humidification is the process of adding water vapor and/or vaporized water to an airstream. Researchers investigated the performance of humidifiers experimentally at low pressures (below atmospheric pressure) to find the impact of operational parameters under unconventional conditions **(Rahimi-Ahar et al., 2018)**. Investigations on the humidification-dehumidification behavior of desiccants via air bubbling in calcium chloride solutions at different temperatures, humidities, and concentrations were reported by **(Guan et al., 2021).** Bubble column technologies have emerged as promising solutions due to their unique ability to localize heat at the air-water interface and reduce heat loss, thereby providing an advanced platform for highly efficient evaporation and steam generation. Some approaches focused on developing humidified solar collectors to reduce the mass of liquid water within the collector, thereby accelerating the attainment of the required evaporation temperatures and minimizing thermal resistance **(Welepe et al., 2022)**. As part of the design development process, hybrid systems integrating HDH units using solar stills integrated with helical humidifiers were tested to enhance operational compatibility **(Kabeel et al., 2022)**.

Numerical studies are conducted to simulate double-diffusion natural convection within an inclined rectangular cavity that mimics a solar still using Computational Fluid Dynamics (CFD) **(Juarez et al., 2015).** The effects of thermal radiation and conduction in the glass cover, along with the effects of angle and aspect ratio on flow patterns and heat and mass transfer within the system, were considered. CFD is employed to simulate heat and mass transfer between the water surface and the moist air stream, to understand evaporation phenomena at sensible-heat equilibrium in the prism cavity **(Chen et al., 2021);** in a tubular cavity with latent heat **(da Silva Junior et al., 2023)** or analyzing the spray rate in a solar distillatory with PCM **(Bahramei et al., 2025).**

Furthermore, to improve component efficiency, the integration of bubble columns with improved solar collectors featuring turbulators has been tested to simultaneously raise the temperatures of the air and water before they enter the humidifier, thereby enhancing the gain out ratio (GOR) **(Rajaseenivasan et al., 2016)**. Bubble-column humidifiers have high heat and mass transfer coefficients due to their small element sizes **(Abd-ur-Rehman et al., 2016).** They studied the effects of air-water superficial velocity, air pressure, water column height, and water inlet temperature on the evaporation process in the humidification module. Results showed enhancement in water evaporation intensity with increasing inlet water temperature and superficial velocity. **(Shaikh and Ismail 2023)** improved the HDH gain output ratio (GOR) and the dehumidifier effectiveness by two-stage bubble column configuration compared to single stage. The achieved water yield, which meets drinking water quality standards, was 4.57 kg/m^2/day, GOR was 0.79, and the estimated cost was 0.0716 USD/liter.

Several studies were conducted to improve freshwater production in solar HDH desalination systems. **(Mahmoudi et al., 2025)** used metal scrap-based porous media and a parabolic dish collector to evaporate water from a stream of air in the humidifier chamber. The results showed that the optimal metal scrap porosity was 0.975, producing about 4 L/day of freshwater. **(Tiwari and Kumar 2025)** integrated a solar thermal HDH system with solar water and air heaters as preheating sources. The humidifier is packed with coconut fiber due to its wettability, low cost, and to improve heat and mass transfer and enhance freshwater productivity. The system achieved a freshwater production rate of up to 5.34 L/h with a maximum thermal efficiency of 46.8%, while producing high-quality water with over 99.6% removal of major dissolved contaminants. Furthermore, the system demonstrated low freshwater production costs and significant environmental benefits through reduced CO_2 emissions.

Recent improvements in HDH systems are reported by **(Alnaimat et al., 2025),** who used ultrasonic atomization with solar harvesting, achieving an enhanced recovery ratio of 68.4%. **(Ziauddin et al., 2025)** achieved a daily yield of 13.38 liters of freshwater by adopting a closed-loop operation. **(Messaouda et al., 2026)** investigated enhancing a humidification-dehumidification system using clay-based water-evaporation elements supported by phase change material to improve evaporation performance at low cost and found a sustainable solution. Consequently, this work aimed to contribute to the ongoing development of the humidification process by proposing a solar humidification system based on dropwise evaporation. It is integrated with air and saline water solar collectors to preheat the ambient air and saline water, respectively.

Even though solar (HDH) desalination systems reported a significant advancement, an obvious research gap regarding the solar dropwise evaporation where a created interfacial simultaneous localized, heat and mass transfer. Previous studies count on decoupled solar thermal collection element from the vapor generation one, leading to a successive thermal loss. Other studies relied on film-wise continuous fluid distribution over the heated surface, which severely limits the performance of evaporation.

To overcome these limitations, this study introduces a novel operational concept that directly merges absorbing solar radiation and water evaporation within a single surface. Specifically, this work coupled the exact fluid-dynamic and thermodynamic behaviors of discrete dropwise evaporation over an unflooded, directly irradiated black flat absorber plate or a hemispherical dimpled absorber. Furthermore, a novel solar air heater configuration is introduced in which the driving air stream is preheated through a confined, forced flow in an S-path along a glazed passage inserted with internally black baffles. This work provides a detailed experimental evaluation of solar thermal evaporation of different dripping rates of water drops on a flat and dimpled absorber geometries. The effect of various air flowrates under real transient outdoor conditions on the evaporation process and on the relative humidity and temperature for the exit air. Water and air are preheated by flat plate solar collector and a novel air solar collector respectively. The present system is solar powered for zero electrical power consumption and supports sustainable goals. collaboratively enhance convective mass transfer coefficients under real transient atmospheric conditions.

2. METHODOLOGY

2.1 Experimental Setup

A schematic diagram of the designed, prepared and instrumented testing apparatus is shown in **Fig. 1a**, illustrates the primary system components with flow paths. **Fig. 1b** shows the matching photograph, illustrating the system's physical layout, including the solar air collector (SAH), flat-plate solar water collector (FPC), solar humidifier, and solar PV power panels, along with the electric and control panels.

This arrangement leads to appropriate operational flexibility. Saline water is heated in flat-plate water solar collectors before being fed to the dropwise supplier unit in the humidifier. Working on the principle of an open loop, an ambient air stream is extracted by an axial fan and introduced into the air solar heater; then a heat and mass transfer mode is actuated in the humidifier between the hot water drops and the hot air stream to produce a stream of air with an elevated moisture content. To maximize air humidification efficiency, the amount of water drops fed to the humidifier is controlled based on available thermal energy and droplet evaporation time. An auxiliary solar PV panel (Model: Hi-MO 6 - LR5-72HBH-645M, Manufactured by LONGi Green Energy Technology Co., Ltd., Xi'an, China) was integrated into the system configuration for the purpose of actuating the axial fan, water pump, and solenoid valves, ensuring an autonomous operation independent of the electrical grid. The PV panel specifications are given in **Table 1.** The humidifier is fabricated from a galvanized sheet of 1.63 mm thickness as a rectangular box, with five sides thermally insulated with 50 mm glass wool. In contrast, the upper side is covered with a 4 mm-thick glass panel to receive solar radiation. Direct solar energy enters through the glass cover and is absorbed by the blackpainted copper absorber (flat-plate and dimpled plate) of dimensions (998 mm × 328 mm × 1 mm). The upper portion of the glass cover is bored with three 3mm-diameter holes for installing the water-dripping unit.

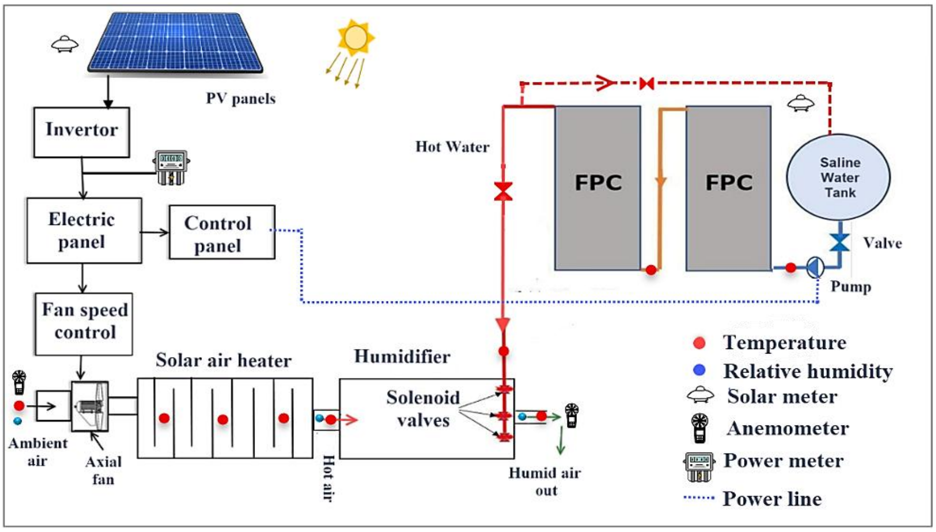

(a)

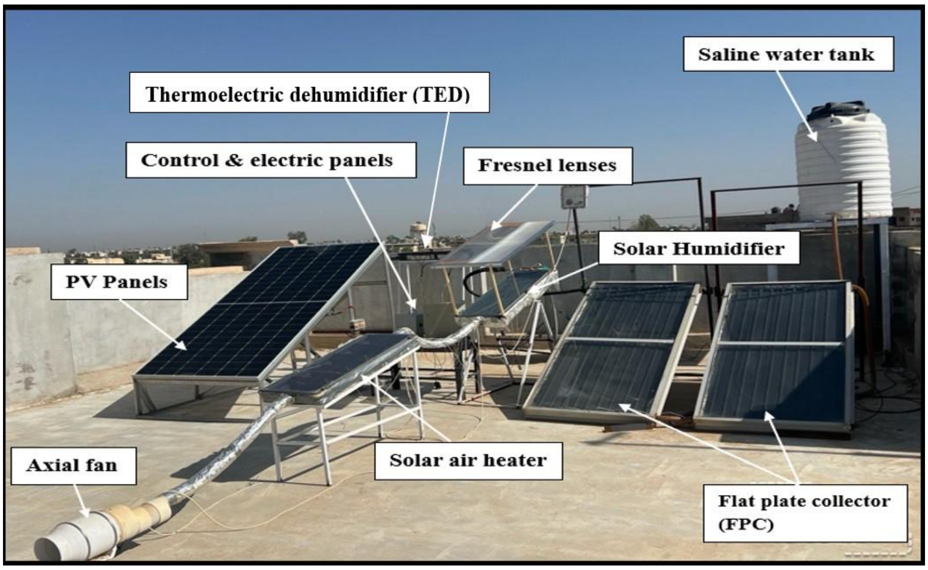

(b)

Figure 1. Experimental test rig; a) Schematic diagram, b) Photographic view.

Table 1. Solar panel characteristics

Parameter	Value
Solar PV-panel dimensions, (mm)	(1110 × 2360 × 30)
PV area, (m^2)	2.62
Maximum power point of the panel, (W)	645
$I_{mp,ref}$, current at maximum power point, (A)	14.4
Reference temperature, (°C)	25
Voltage open circuit, at reference conditions, (V)	54.12
Short-circuit current at reference conditions, (A)	15.06

The solar air collector is connected to the humidifier inlet via a flexible tube. The size of the humidifier and air heater was (1000 mm x 330 mm x 50 mm), as given in **Table 2.** The comprehensive range of experimental operating conditions adopted in this work is presented in **Table 3**. Three Micro Sphygmomanometer Solenoid Valves, shown in **Fig. 2a**, are used to ensure precise volumetric dosing and highly regulated dropwise water distribution onto the absorber plate.

Table 2. Specifications of the solar humidification system

Element dimensions (mm)	Element	Material	Thickness, (mm)
Humidifier of (1000 × 330 × 50)	Absorber plate (flat or dimpled) Top side Side walls and bottom are thermally insulated, (mm)	Copper Glass panel Glass wool	1 4 50
Solar air collector of (1000 × 330 × 50)	Absorber plate Baffles Number of baffles = 8 Collector top side Thermal insulation of side walls and bottom, (mm) Axial fan of 75 W power, and max flow rate of 9 m^3.min	Copper Copper Glass panel Glass wool	1 1 4 50 -
Water solar flat-plate collectors of (1920 × 850 × 100)	Quantity: 2 in series connection Absorber plate cover Risers' material diameter Number of risers = 10 Thermal insulation for edge and back sides Water tank of (500 liter) capacity Pump of 75 W power, 2.8 max head, max flow rate of 1400 lph	 Copper Glass panel Aluminum Glass wool PVC	 1 4 10 50 1.5

Table 3. The experimental operational parameters (units tilt angle is 30°).

Parameter	Range
Ambient temperature	between 25.7 °C at 8:00 and 37.8 °C at 15:00 according to the test day
Humidifier inlet air temperature	30 °C at 8:00 to 60 °C at 12:00 according to the test date
Inlet water temperature to FPC	16.3 at 8:00 to 38.7 °C at 12:00 according to the test date
Ambient relative humidity HR	between 17.7% at 8:00 and 5% at 13:00 and 22.3% at 22:00 according to the test day
Air flowrate (m^3/min)	0.5, 0.75, 1, 1.5
Water dripping rate (drops/s)	4, 7, and 10

These components were explicitly integrated using the low-pulse Micro-Sphygmomanometer Solenoid Valves (Model: 1714DC3V, Manufactured by Shenzhen Skoocom Electronic Co., Ltd., Guangdong, China). Operating at a nominal voltage of 6 VDC and a rated power consumption of 1.5 W, these high-frequency micro-valves were actuated via a decoupled Arduino control loop to maintain a uniform dripping frequency across varying operational flow rate testing cycles. A programmable Arduino controller controls valve operation to manage the opening and closing sequence. The control system used in this work, shown in **Figs. 2b-2e**, ensures high processing speed and eliminates computational latency. A dual-microcontroller architecture consists of two separate Arduino boards working in parallel. The first Arduino Uno R3 is dedicated exclusively to executing the timing loops and pulse frequencies required to actuate the micro-sphygmomanometer solenoid-dripping valves for precise water distribution. To streamline the system description, water dispersion is controlled by a DC 3-5V solenoid valve with a power consumption of < 2W. This compact unit has structural dimensions of 25 × 14.4 mm, with inlet/outlet port diameters of 3.9mm and 2.9mm, respectively.

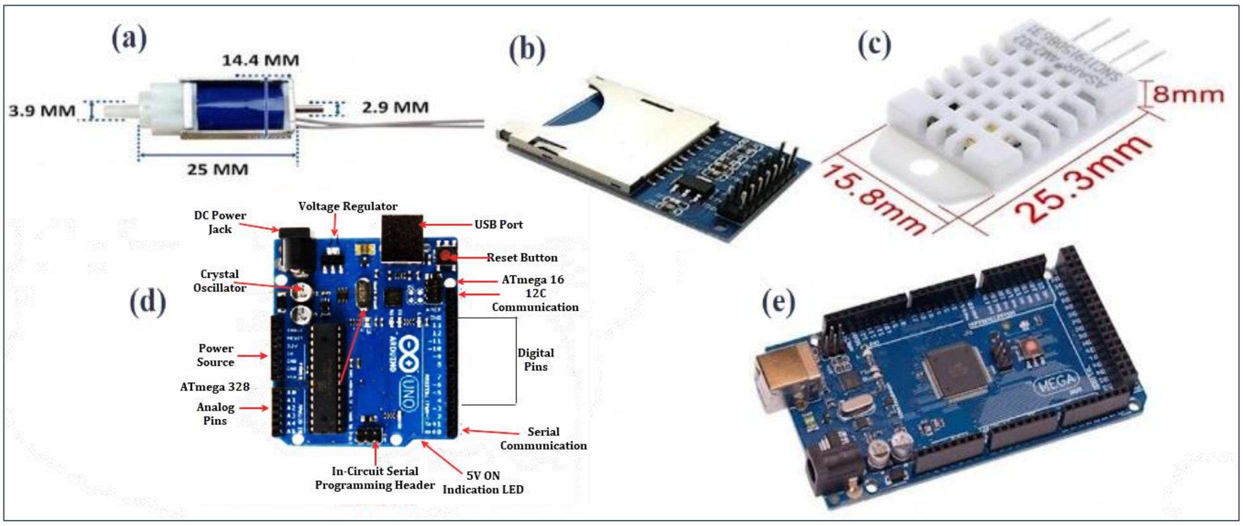

Figure 2. Control system includes a) Micro sphygmomanometer solenoid valve, b) SD Card Module, c) DHT22 digital sensor, d) Arduino Uno R3, and e) Arduino Mega 2560 R3.

Mechanistically, the valve operates over a pressure range of 0-350 mmHg, ensuring precise timing and volumetric control of the water droplets discharged onto the absorber plate.
Concurrently, the second, completely independent Arduino Mega 2560 R3 is deployed solely for high-frequency data acquisition, managing the real-time continuous signals from the digital capacitive humidity and temperature sensors (DHT22). This physical decoupling of tasks ensures that the continuous scanning of environmental variables does not introduce execution delays or electrical cross-talk into the water-side dripping control loop. This monolithic design isolates the sensing and recording operations from the mechanical actuation of the valve, thereby improving control stability and measurement accuracy during solar humidification tests **(Rastogi, 2021; Sánchez-Sutil and Cano-Ortega, 2021)**.
The measured parameters during the tests were inlet and outlet temperatures for water and air solar collectors, ambient temperature, and the temperature at the exit of the solar humidifier; incident solar radiation; air velocity; and relative humidity at the humidifier entrance and exit as presented in **Fig. 1a**. The experimental setup was installed in Baghdad, Iraq (33.3° N, 44.3° E), and tested in October 2025.
Twelve K-type thermocouples were used in this work; five are located at the inlet, outlet and on the absorber plate of the solar air collector. Three sensors are used for water solar collectors to measure the water temperatures at their inlets and outlets. Two are used to measure the temperature at the absorber of the humidifier, one at its outlet, and one for ambient temperature. The thermocouples were connected to a 12-channel data logger (Lutron BTM-4208SD) with an accuracy of ±2.5%. This specific hardware was used solely for temperature data logging.
At the inlet and outlet of the humidifier, relative humidity (RH) was measured using DHT22 sensors interfaced with an Arduino Mega 2560 R3 board and stored on an SD card. Air volumetric flow rate (Q) was calculated according to:

$$Q = v \times A \quad (1)$$

where:
v is air measured velocity (m/s)
A is the inlet area of the humidifier (m^2); it is calculated as (a × b), where a and b are the height and width of the duct, (m).
Measurements of velocity with a hot-wire anemometer (Model: TES-1340, Manufactured by TES Electrical Electronic Corp., Taipei, Taiwan) are used. Temperature sensors were calibrated for sensitivity detection and connected to a data acquisition unit (Lutron BTM-4208SD). Data acquisition was performed every 15 minutes over nine hours (from 8:00 AM to 5:00 PM). The technical data for the sensors and measurement probes used in the experimental setup are given in **Table 4.**

Table 4. Instruments with range and accuracy.

SI.no	Variable	Model, device	Accuracy	Range
1	Temperature	K-type thermocouple	±1 ℃	-100 – 1300℃
2	Solar energy	TES,1333R solar meter	±10W/m^2	0–2000 W/m^2
3	Air velocity	TES,1340 Anemometer	±0.1 m/s	0 – 30 m/s
4	Relative Humidity	DHT22 sensor	±2%	0 – 100 %

2.2 Theoretical Model

The saturation vapor pressure (P_{sat}) is calculated at the measured air temperature (T) **(Cengel, 2006)**

$$P_{sat} = 0.61121 \times exp\left(\frac{17.67 \cdot T}{T+243.5}\right) \quad (2)$$

The actual vapor pressure (P_v) is derived from the measured relative humidity (RH);

$$P_v = \frac{\mathrm{RH}}{100} \times P_{sat} \quad (3)$$

Air humidity ratio (w) is calculated based on the partial pressure of water vapor and atmospheric pressure **(Kays et al., 2004),** such as:

$$w = 0.622 \times \frac{P_v}{P_{atm} - P_v} \quad (4)$$

where P_{atm} is the atmospheric pressure.
The mass balance describes the conservation of mass within the humidifier (evaporation chamber), which can be written as **(Cengel, 2006):**

$$\dot{m}_a \times w_{in} + \dot{m}_{w,in} = \dot{m}_a \times w_{out} + \dot{m}_{w,out} \quad (5)$$

where $\dot{m}_a$ is the air mass flow rate, kg/s.
$\dot{m}_w$ is the water mass flow rate, kg/s.
The evaporation rate ($\dot{m}_{evap}$) is determined by the difference in humidity ratio between the inlet and outlet;

$$\dot{m}_{evap} = \dot{m}_a \times (w_{out} - w_{in}) \quad (6)$$

while air enthalpy is calculated as:

$$h = 1.006 \times T + w \times (2501 + 1.86 \times T) \tag{7}$$

The latent heat of evaporation (h_{fg}) is evaluated by: **(Rahbar and Esfahani, 2012a; 2012b)**:

$$h_{fg} = 2.495 \times 10^6 \times [1 - (9.4749 \times 10^{-4}T + 1.3132 \times 10^{-7}T^2 - 4.7947 \times 10^{-9}T^3)] \tag{8}$$

where T is water temperature delivered from the Flat Plate Collector (FPC) before the dropwise vaporization process, which corresponds directly to the inlet water temperature entering the humidifier channel. To ensure numerical high fidelity, this polynomial formulation exhibits a Mean Absolute Error (MAE) of less than 0.15% (≤ 3.72 kJ/kg) when validated against standard thermodynamic steam tables within the operating temperature spectrum.

The overall energy balance for the humidifier is shown in **Fig. 3** and given as:

$$Q_{solar} + Q_{in} = Q_{out} + Q_{loss} \tag{9}$$

where Q_{solar} is the solar radiation is received by the humidifier (W). It is evaluated as:

$$Q_{solar} = I \times A_H \times \tau_g \times \alpha_p \tag{10}$$

I is the incident solar radiation, W/m²
A_H is the aperture area of the humidifier (it is equal to 0.33 m²)
τ_g is the transmissivity of the glass cover =0.9
α_p is the absorptivity of the copper plate =0.95

The energy balance given in Eq. (9) can be applied for both flat-plate and dimpled absorbers shown in **Fig. 3a**. So, Eq. (9) can be rewritten as:

$$I \times A_H \times \tau_g \times \alpha_p + \dot{m}_a \times h_{a,in} + \dot{m}_{w,in} \times h_{w,in} = \dot{m}_a \times h_{a,out} + \dot{m}_{w,out} \times h_{w,out} + Q_{loss} \tag{11}$$

The humidifier's effectiveness (ε_{hum}) is evaluated based on the actual difference in air humidity ratio about the humidifier relative to the maximum difference between the saturation and the inlet humidity ratio, such as **(Kabeel et al., 2022)**:

$$\varepsilon_{hum} = \frac{w_{out} - w_{in}}{w_{sat,out} - w_{in}} \tag{12}$$

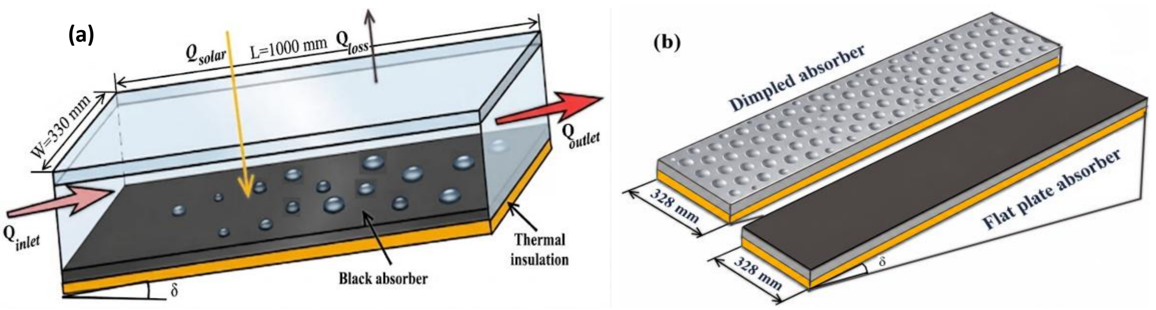

Figure 3. Schematic configurations of the solar humidifier: a) thermal energy balance for the humidifier, b) geometry of absorber plates.

Air pressure drops (ΔP) in the solar humidifier can be evaluated using the Darcy-Weisbach equation given as: **(Kays et al., 2004)**

$$\Delta P = f \cdot \left(\frac{L}{D_h}\right) \cdot \left(\frac{\rho \cdot v^2}{2}\right) \tag{13}$$

where
L is duct length, m.
ρ is air density at the humidifier inlet temperature, kg/m^3.
D_h is the humidifier hydraulic diameter, (m).

$$D_h = \frac{4\times(flow\ area)}{wetted\ perimeter} \tag{14}$$

The hydraulic diameter is calculated as:

$$D_h = \frac{4\times(a\times b)}{2\times(a+b)} \tag{15}$$

f is the duct friction factor. It is evaluated based on the Reynolds number ($Re = \frac{\rho \dot{V} D_h}{\mu}$)
The friction factor for the humidifier with a flat absorber and a dimpled absorber is calculated based on laminar air flows (since the Reynolds number varies from 2280 at 8:00 to 2140 at solar noon for an air flow rate of 0.5 m^3/min) as:

$$f = \begin{cases} \frac{45}{Re} \ (\textbf{Shah and London}, \textbf{1978}) for\ flat\ plate \\ f\ is\ taken\ from\ Fig.12\ of\ (\textbf{Kaood et al.}, \textbf{2019}) for\ dimpled\ plate \end{cases} \tag{16}$$

ρ is air density at the humidifier inlet, kg/m^3.
μ is air dynamic viscosity, Pa.s.

2.3 Uncertainty Analysis

To ensure the reliability and accuracy of the experimental results, an uncertainty analysis was performed. The total uncertainty of the measured parameters arises from the limitations of the measuring instruments, their calibration, and environmental fluctuations. The accuracy of the sensors used in this study, including the K-type thermocouples (±0.5 ℃), the DHT22 humidity sensor (±2%), and the solar power meter (±5%), was considered. For the calculated parameters (R), such as the humidification effectiveness or heat transfer rates, the uncertainty was estimated using the propagation of error method proposed by **(Kline and McClintock 1953; Dizaji et al., 2023)** as:

$$U_R = \left[\left(\frac{dR}{dx_1}U_1\right)^2 + \left(\frac{dR}{dx_2}U_2\right)^2 + \cdots \left(\frac{dR}{dx_n}U_n\right)^2\right]^{0.5} \tag{17}$$

Where, U_R is the total uncertainty in the result, x_1 , x_2 , ..., x_n are the independent variables. U_1 , U_2 , ..., U_n are the uncertainties of the individual measurements.
Using the error-propagation method described in Eq. (17), the experimental uncertainty margins for the key computed thermodynamic parameters were rigorously determined. The calculated uncertainties for the air mass flow rate ($\dot{m}_a$) and water mass flow rate ($\dot{m}_{w,\,in}$) ranged from ±1.2% to ±2.4% and ±0.8% to ±1.5%, respectively. Consequently, the propagating uncertainty for the local air humidity ratio (w) was found to span between ±2.1% and ±3.8%. In contrast, the uncertainty range for the estimated thermal heat transfer rates (Q) was bounded within ±3.2% to ±4.7%. Ultimately, the maximum accumulated uncertainty for the overall humidifier effectiveness (ε_{hum}) did not exceed ±5.2%, which falls well within the acceptable technical limits (≤5%) commonly prescribed for high-fidelity solar thermal desalination instrumentation systems.

3. RESULTS AND DISCUSSION

3.1 Environmental Conditions

A set of experiments was conducted on clear-sky sunny days in October 2025, under Baghdad (33.07° N, 44.35° E) meteorological conditions for comprehensive evaluation. The tests were repeated to evaluate the effect of airflow rates of 0.5, 0.75, 1, and 1.5 m^3/min on the performance of a solar humidifier tilted at δ equals 30° using flat and dimpled absorbers with a 1 mm plate thickness.

Fig. 4 shows the meteorological conditions, including hourly solar radiation and ambient temperature, for the five testing days in October 2025 for the HD. In **Fig. 4a**, the solar intensity over selected days showed minimal variation, averaging 510-550 W/m^2, indicating negligible differences in solar radiation levels during the observation period.

The average solar intensity (I_{avg}, W/m^2) during the steady-state testing was compiled utilizing the arithmetic mean formulated as follows **(Duffie et al., 2020)**:

$$I_{avg} = \frac{\sum_{i=1}^{n} I_i}{n} \tag{18}$$

where I_i represents the instantaneous global solar radiation measurements logged at equal, discrete time intervals (Δt = 15 min), and n is the total number of recorded samples.

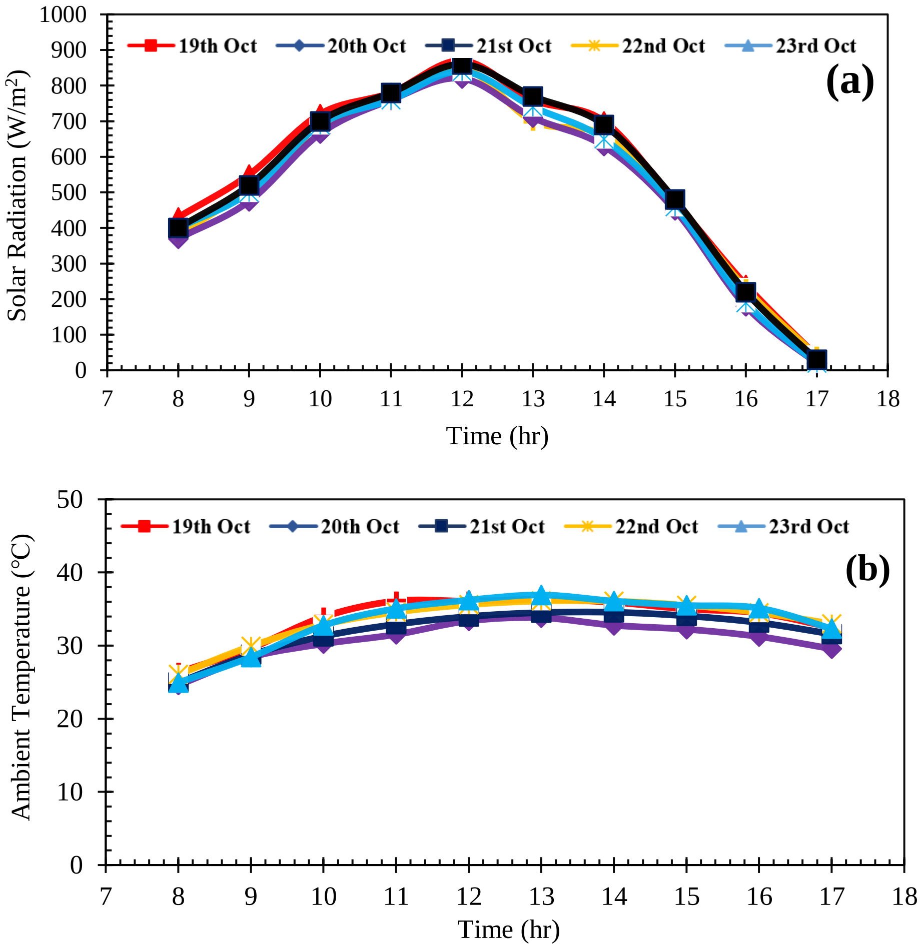

Figure 4. Hourly ambient conditions for days 19th to 23rd in October 2025, a) Solar radiation, b) Ambient temperature.

Similarly, the ambient temperature ranged from 24 to 26°C at 8:00, increased to a peak of 34 to 36°C at 12:00, and then declined to 29.5 to 29.5–32.5°C at 17:00, as shown in **Fig. 4b**. Higher solar radiation leads to greater energy input to the system elements (the flat-plate water collector, the solar air collector, and the solar humidifier), thereby resulting in higher distilled water productivity.

3.2 Water Flat-Plate Collector (FPC)

The hourly temperatures for the flat-plate water collectors are presented in **Fig. 5** for a selected day. All three temperatures (Tw_{in}, Tw_m, Tw_{out}) follow a perfect bell curve, closely mirroring the solar irradiance pattern. This confirms that the solar collector is functioning correctly and is the primary driver of the water temperature. The collector successfully adds a substantial amount of thermal energy to the water. The outlet temperature (Tw_{out}) rises from approximately 40°C in the morning to a peak of around 90-94°C at midday. Throughout the day, there is a consistent, clear temperature difference between the inlet, midpoint, and outlet ($Tw_{out} > Tw_m > Tw_{in}$). This indicates that heat is being efficiently transferred from the collector's absorber plate to the water and that the water is not stagnating; it flows continuously, allowing a steady-state temperature gradient to exist along the length of the collector.

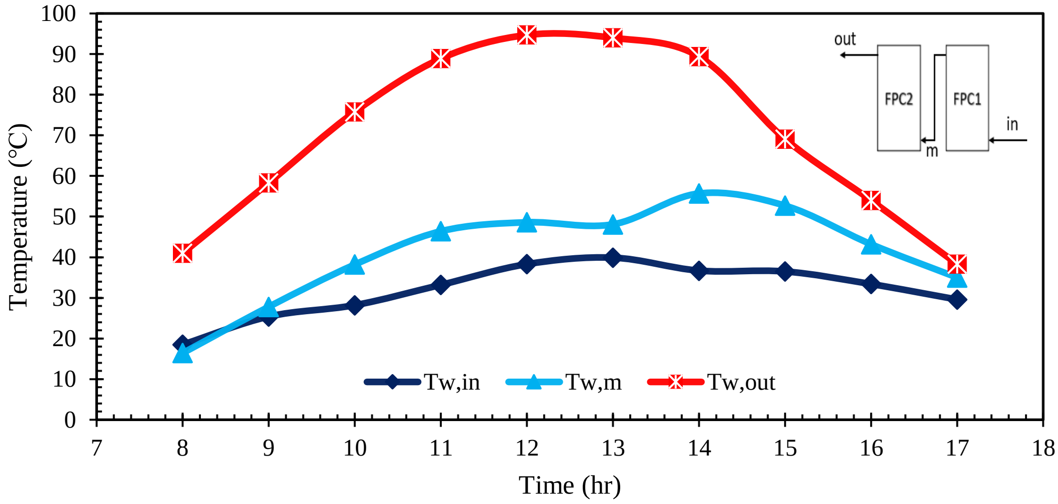

Figure 5. Inlet, mean, and outlet saline water temperature of FPC on 19th October.

3.3 Solar Air Collector

In a solar air collector equipped with turbulators, the outside air (solar collector) temperature increases due to turbulence created in the flow field of the collector **(Rajaseenivasan and Srithar, 2016)**. **Fig. 6** illustrates the primary counter relationship between exit air temperature and air mass flow rate. This trend is governed by air residence time and thermal dilution. Increasing the airflow rate from 0.5 to 1.5 m^3/min reduces the peak temperature from 74 ℃ to 60 ℃–62 ℃. Physically, lower flow rates prolong the fluid residence time, maximizing heat accumulation. Conversely, higher flow rates distribute the constant solar insolation over a larger air mass flux, inducing a thermal dilution effect that depresses the peak discharge temperature due to the distribution of solar insolation over a greater quantity of flowing at least partially heated air; yet this directly impacts the downstream humidification step where warmer, Physically, a lower relative humidity and high temperature of air enhance the moisture-carrying capacity of the flowing stream by maximizing the vapor pressure differential between the air and water droplets. This elevated concentration gradient serves as the primary driving force for accelerated mass transfer, directly increasing the evaporation rate and boosting the system's cumulative distillate productivity.

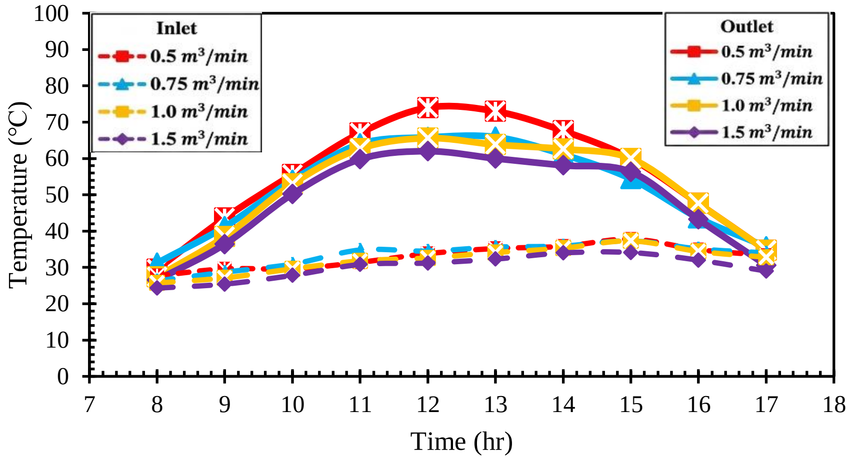

Figure 6. Hourly outlet and inlet air temperature of the solar air collector for different air flow rates.

3.4 Impact of Water Flow Rate on Air Saturation

The effect of water drip rate on the outlet relative humidity (RH_{out}) of the solar humidifier was tested at a fixed air flow rate of 0.5 m^3/min, as shown in **Fig. 7**. The findings show that water drip rate has a negligible effect on RH_{out}. At a drip rate of 4 drops/s, the relative humidity remained low because the contact surface area between water drops and air, and between water drops and the absorber plate, was insufficient for heat and mass transfer to saturate the airstream. However, the outlet relative humidity reached about 75% when the drip rate was increased to 7 drops/s (i.e., a water flow rate of 0.297 g/s), indicating a notable improvement. This improvement results from a faster evaporation rate due to a larger contact area between the hot water drops (96°C) and the air stream.

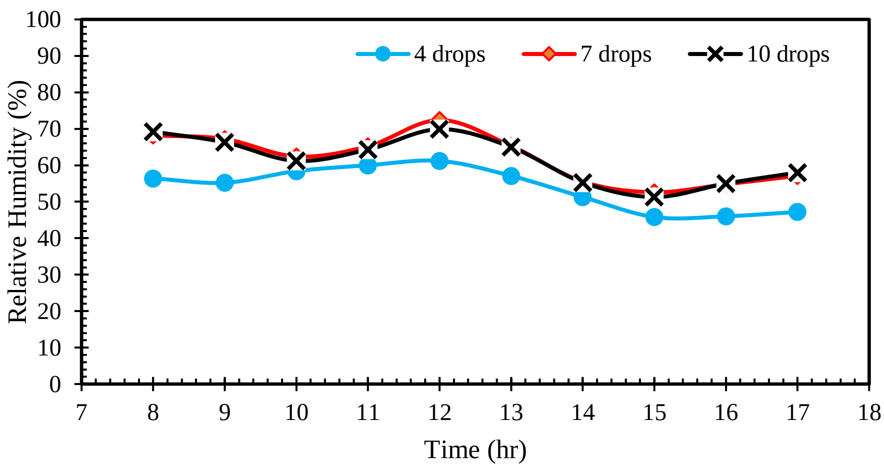

Figure 7. Hourly air relative humidity for different water dripping rates at the exit of the solar humidifier

It is interesting to note that little or no increase in RH_{out} was observed at 10 drops/s (0.423 g/s) with larger drop sizes; conversely, a steep decrease or stability in humidity was observed. This was due to two reasons: first, coalescence, in which a higher density of 3-mm droplets resulted in more collisions and thus a lower air-liquid surface-area-to-volume ratio. Secondly, the excess water mass might have led to a slight decrease in the humidifier's air temperature due to reduced moisture-holding capacity. Therefore, a 7 drops/s (0.297 g/s) drip rate was determined to be the optimal operating point, achieving an appropriate trade-off between droplet residence time and heat exchange for near-complete air saturation. The relative humidity of the air at the humidifier inlet (RH_{in}) corresponds directly to the exit conditions of the solar air collector. Due to the high-temperature elevation within the solar collector, the air's relative humidity dropped significantly, resulting in very low and closely clustered RH_{in} values across all testing days. This low relative humidity indicates a high thermal capacity and a severe moisture deficit in the air stream, which serves as the driving force to maximize the dropwise evaporation rate when the air interacts with the dimpled absorber plate inside the humidification chamber.

3.5 Impact of Air Flow Rate on Air Saturation

The relative humidity at the solar humidifier inlet (RH_{in}) shown in **Fig. 8** indicates a clear, consistent trend across the different airflow rates. The humidity ratio does not change with heating; thus, the cooler air has higher relative humidity. The main thing to note is that these values are constant over time: at a given flow rate, the behavior is consistently flat, meaning the air entering the humidifier is in stable condition at any given moment.

This stability is essential for the validity of the comparative analysis of outlet relative humidity (RH_{out}) from the humidifier. The baseline RH target value, $RH_{in,}$ for each flow level serves as a stable, independent reference. Any significant deviation in the moisture gain ($RH_{out} - RH_{in}$) can be assigned directly to the action of the humidifier itself, such as, e.g. its absorber plate geometry and thickness, rather than being obscured by variations in the inlet air temperature.

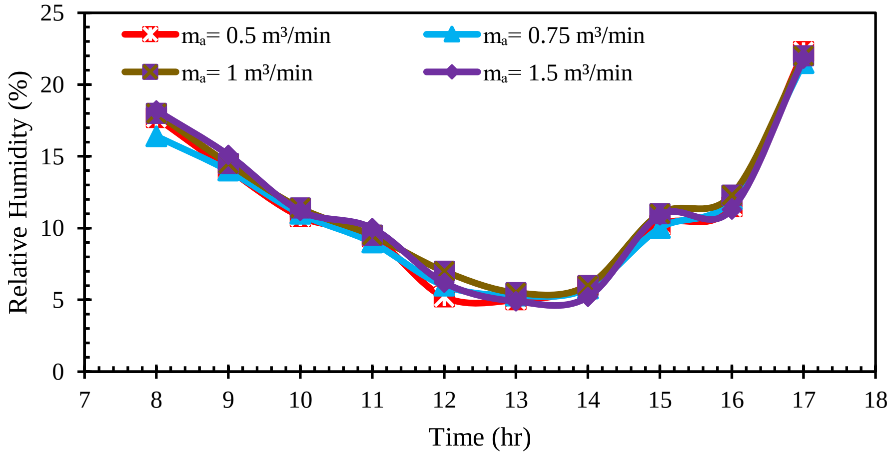

Figure 8. Hourly variation of air relative humidity at the solar humidifier inlet for the tested air flow rates.

Figs. 9a and 9b show the diurnal variation of outlet and inlet relative humidity for the solar humidifier with flat (case-I) and dimpled (case-II) absorbers at different air mass flow rates and a dripping rate of 7 drops/s (0.297 g/s). An inverse relationship between the air flow rate and the evaporation rate, as indicated by RH_{out} is observed. The highest outlet RH for case I was (75%), while that for case-II was (85.6%), corresponding to the lowest air flow rate (0.5 m^3/min).

Since lowering the air flow rate allows the air to spend more time inside the humidifier, it permits the air stream to attain thermal equilibrium with the water droplets, thereby enhancing evaporation and raising air humidity. On the other hand, at an air flow rate of 1.5 m^3/min, the maximum RH_{out} decreased steeply to about 45% for case-I and 64.1% for case-II. This decrease is attributed to reduced contact time between air and water drops, which is insufficient to evaporate the drops and saturate the airstream. The increased flow rates lead to a decrease in outlet air temperature as outlined previously, and cooler air has lower saturation vapor pressure, holding less moisture at the same time (which underscores that the maximum attainable relative humidity can be limited even if absolute humidity increases).

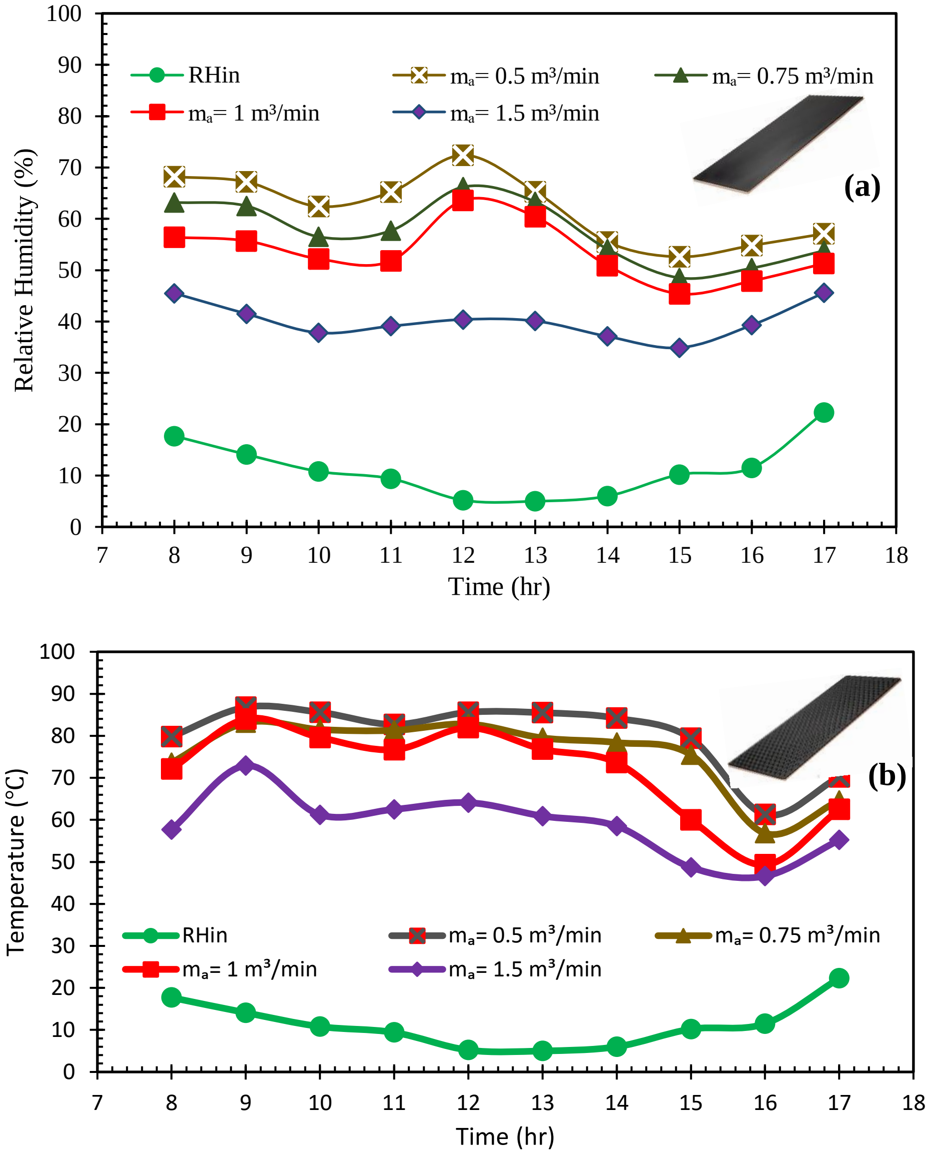

Figure 9. Hourly variation of inlet and outlet relative humidity at the solar humidifier exit for different air flow rates, a) flat absorber, b) dimpled absorber.

This balance between mass transfer kinetics and thermodynamic equilibrium introduces a key trade-off: low flow rates produce air streams with higher relative humidity, but high flow rates treat a larger mass of air. Consequently, the optimal flow rate for the humidifier system is not the one that maximizes RH_{out} alone, but the one that maximizes the total mass of water vapor produced, which is the product of the air mass flow rate and the outlet air's specific humidity (absolute moisture content).

Figs. 10a and 10b illustrate the impact of air flow rate on the humidification effectiveness (ε_{hum}) for cases I and II. The highest humidification efficiency was consistently achieved at the lowest flow rate of 0.5 m^3/min, reaching 70% and 85% for cases I and II, respectively. This superior performance at low velocities is attributed to the extended residence time of air over the wetted absorber plate, which facilitates more effective air-water interaction and evaporation. Conversely, as the air flow rate increased to 1.5 m^3/min, the effectiveness significantly deteriorated to 37% for case I and 52% for case II due to a reduction in water-air contact duration, which reduced evaporation. Notably, while the effectiveness decreases with higher air flow rates, the overall evaporated mass transfer is enhanced for case II compared to case I (as shown in **Figs. 9b and 10b**) due to the larger surface area of the dimpled absorber compared to the flat one, permitting a better interaction between the air stream and water droplets. Also, the dimple geometry enhances turbulence intensity, which supports the evaporation process and flow mixing, consequently leading to a positive impact on heat and mass transfer.

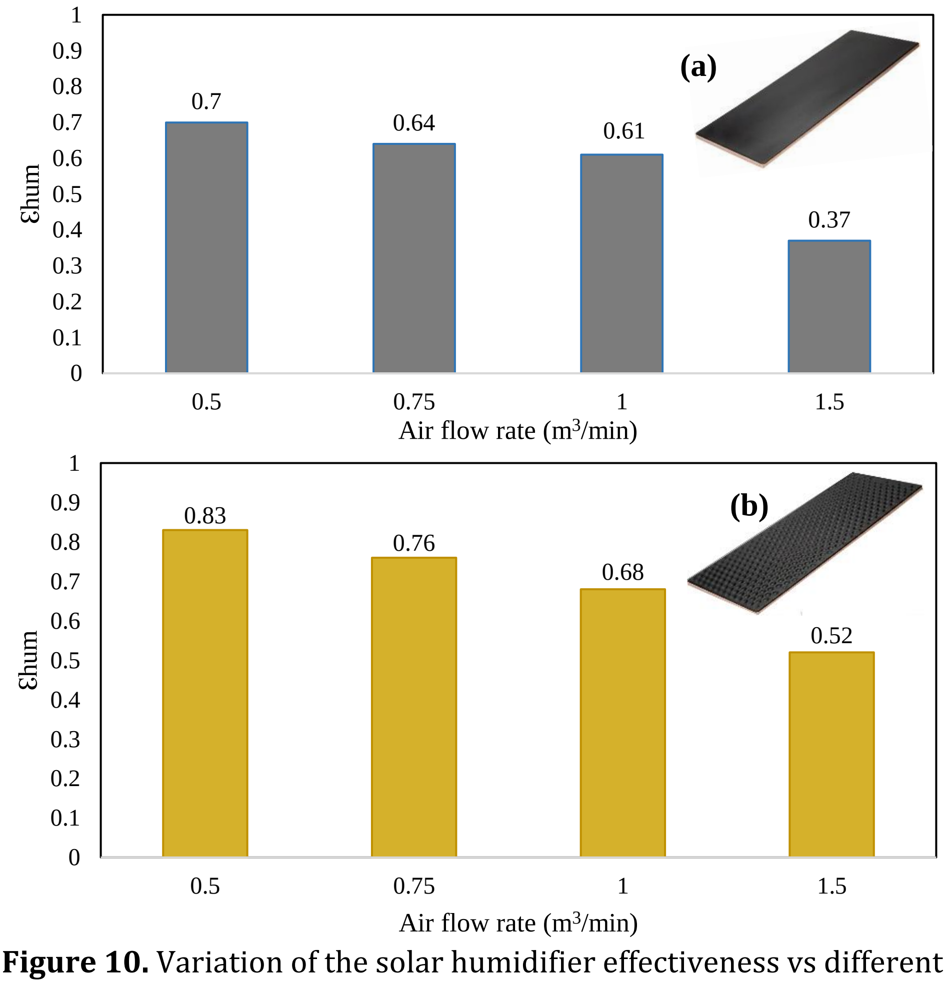

Figure 10. Variation of the solar humidifier effectiveness vs different air flow rates for: a) flat absorber, b) dimpled absorber.

3.6 Hydraulic Penalty and Temporal Pressure Drop Variation

To satisfy the hydrothermal performance criteria, the transient pressure drop (ΔP) across both the flat and dimpled passages was rigorously monitored and analyzed. **Fig. 11** illustrates the temporal variation of ΔP throughout the operational hours (from 8:00 to 17:00) at a constant volumetric air flow rate of 0.5 m^3/min. For the baseline flat-plate channel, the aerodynamic resistance remained exceptionally minor and stable, fluctuating tightly within a narrow margin of 0.08 Pa to 0.13 Pa. This behavior is characteristic of smooth-wall convective passages under transitional flow profiles. Conversely, implementing the dimpled absorber plate resulted in a deterministic increase in the system's flow resistance, with ΔP ranging from a minimum of 0.21 Pa at early testing hours to a peak of 0.36 Pa. Physically, this step-up represents a friction factor enhancement ratio of 2.8. This behavior is primarily attributed to the structural presence of macro-protrusions, which introduce local physical blockages, trigger continuous boundary layer disruption, and induce localized turbulent wake shedding behind the 193 staggered dimples. Crucially, while this structural modification incurs a clear hydraulic penalty compared to the flat-plate configuration, the absolute pressure-drop penalty remains remarkably low (safely below 0.4 Pa). This demonstrates that the high-evaporation process via the dropwise vaporization scheme is sustained with negligible parasitic airflow power consumption, which can be calculated as:

$$\text{Power} = \text{flow rate} \times \text{pressure drop} \tag{19}$$

It is calculated at 12:00 as 3.32 mW for the humidifier with a dimpled absorber.

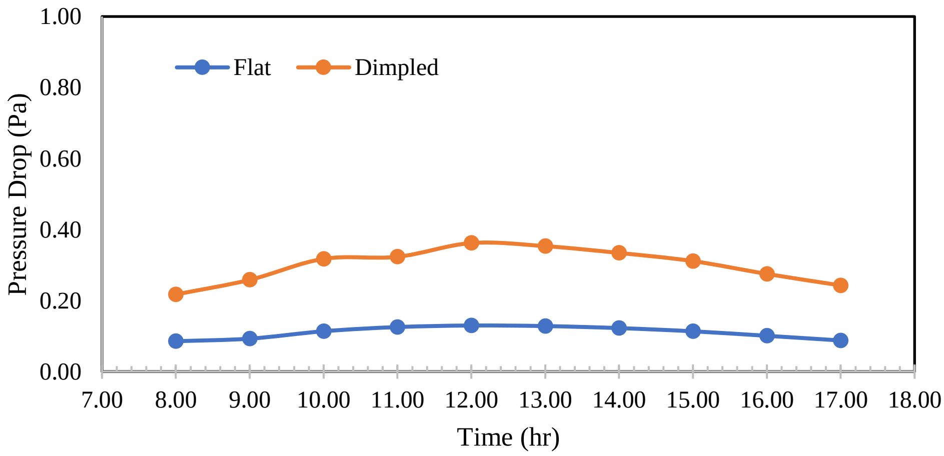

Figure 11. Hourly variation of air pressure drop through the flat and dimpled humidifier passages at the air flow rate of 0.5 m^3/min.

A comparison of the humidifier's effectiveness in the present work with previously published data is presented in **Table 5.** The experimental inclined solar humidifier with falling water drops achieved an average effectiveness of 0.698 with the dimpled absorber and 0.58 with the flat-plate absorber. The dimpled absorber exhibited higher effectiveness than the solar humidifier reported by **(Abdullah et al., 2024)** (0.612) and the packed-bed humidifier investigated by **(Zubair et al., 2018)** (0.54). It also outperformed the packed-bed humidifier studied by **(Shaikh and Ismail, 2023)** (0.66). However, the humidifier's effectiveness remained lower than that reported by **(Essa et al., 2025),** who achieved 0.856 with wheat straw packing material, and slightly lower than the theoretical values reported by **(Wang et al., 2024)**, which ranged from 0.85 to 0.72 depending on the water-to-air mass flow ratio. These results indicate that incorporating a dimpled absorber significantly enhances the performance of the solar humidifier while maintaining a simple design and operation. The present system also demonstrates the feasibility of achieving competitive humidifier performance using solar energy under Iraq's climatic conditions.

Table 5. Comparison of the present humidifier with others

Reference	Nature of the work	Type of the system	Source of energy	Effectiveness of the humidifier	country
(Essa et al., 2025)	Experimental	HDH with wheat straw as packing material	Electrical energy	0.856	Egypt
(Shaikh et al., 2023)	Experimental	Humidifier with packed bed	Solar energy	0.66	India
(Abdullah et al., 2024)	Experimental	Humidifier based on solar distiller	Solar energy	0.612	Egypt
(Wang et al., 2024)	Theoretical	Direct Contact Humidifier	Electrical energy	varied from 0.85 to 0.72 as the water-to-air mass ratio increased from 0.4 to 1.6	China
(Zubair et al., 2018)	Experimental and theoretical	Packed-bed humidifier	Electrical energy	0.54	Saudi Arabia
Present work	Experimental	Inclined solar humidifier with falling water drops	Solar energy	0.58 for flat plate absorber 0.698 for dimpled absorber (average value)	Iraq

4. CONCLUSIONS

The experimental investigation of the solar humidification system demonstrated that the interplay between water-spray dynamics and air flow rates is critical for achieving maximum air saturation. The results revealed that a water drip rate of 7 drops/s (0.297 g/s) is the optimal operating point, yielding a peak outlet relative humidity of 72.4% by providing the best balance between the droplets' interfacial surface area and their thermal residence time. Conversely, increasing the airflow rate from 0.5 to 1.5 m^3/min resulted in a significant decrease in outlet humidity (from 72.4% to 40.4%), confirming that higher airflow rates reduce the residence time required for complete evaporation. Given that water temperatures reached up to 96°C, it is recommended to use variable-speed fans to dynamically synchronize air flow with solar intensity, maintaining high humidity throughout the day. The dimpled absorber delivers noticeably better humidification performance than the flat-plate absorber under all the covered airflow rates. The maximum reported relative humidity was 85.6% at the outlet of the humidifier with a dimpled absorber, compared to 75% for case I, while the humidifier effectiveness was 85% and 70%, respectively, corresponding to an airflow rate of (0.5 m^3/min). Results show thermal performance enhancement by integrating the solar humidifier with dimpled absorber plate compared to conventional flat plate. The system's operational efficacy is inherently governed by fluid residence time and convective thermal dilution, with optimizing the air volumetric flow rate maximizing thermal accumulation at the heated boundaries. Lower inlet humidity ratio directly accelerates evaporation kinetics and increases the cumulative yield.

For future work, the following proposals can be adopted:
1. Investigate the impact of different nozzle designs and droplet sizes.
2. Use an ultrasonic atomizer to explore its effect on evaporation rates within the solar humidifier.
3. Study the effects of coating the absorber with hydrophobic or hydrophilic materials, or of surface texture geometry, on heat and mass transfer, and humidification effectiveness.
4. Use of a multi-stage humidification unit
5. Explore the benefits of integration of sensible or latent thermal energy storage materials to extend the humidification process after sunset or during low solar radiation.
6. Theoretically analyze or conduct computational fluid dynamics simulations of the humidifier to explore the interaction between airflow, heating the absorber, droplet evaporation, and mass transfer inside the humidifier.

NOMENCLATURE

Symbol	Description	Symbol	Description
A	Area, m^2	Q	Volumetric flow rate, m^3/min
h	Enthalpy (kJ/kg)	Q_{loss}	Heat loss, W
h_{fg}	Latent heat of evaporation (kJ/kg)	Q_{solar}	Solar heat, W
I	Incident solar radiation, W/m^2	T	Temperature, (°C)
$m^{\cdot}$	Mass flow rate (kg/s)	Δt	Time interval, (min)
$m^{\cdot}_{evap}$	Evaporation rate (kg/s)	v	Air velocity (m/s)
n	Number of recorded samples	w	Humidity ratio, (kg$_w$/kg$_a$)
P_{atm}	Atmospheric pressure (kPa)	α_p	Absorptivity of the copper plate
P_{sat}	Saturation vapor pressure (kPa)	ε_{hum}	Effectiveness of humidifier (%)
P_v	Actual vapor pressure (kPa)	τ_g	Transmissivity of the glass cover
Abbreviations			
CFD	Computational fluid dynamics	MSF	Multi-stage flash
DB	Dry bulb	PV	Photovoltaic
FPC	Flat plate collector	RH	Relative humidity, (%)
GOR	Grain out ratio	RO	Reverse osmosis
HDH	Humidification-dehumidification	SAH	Solar air collector
MED	Multi-effect distillation	SHD	Solar humidifier
subscript			
a	air	m	mid
avg	average	out	outlet
$evap$	evaporation	sat	saturated
H	aperture area	$solar$	solar
in	inlet	w	Water
$loss$	loss		

Credit Authorship Contribution Statement:

Saad Mohsin Alsaady: Writing original draft, Methodology, and Validation; Karima E. Amori: Writing–review & editing, Methodology, Supervision, and proofreading.

Declaration of Competing Interest

The authors declare that they have no known competing financial interests or personal relationships that could have influenced the work reported in this paper.

REFERENCES

Abdullah, A.S., Elsayad, M.M., Almoatham, S. and Sharshir, S.W., 2024. 6E evaluation of an innovative humidification dehumidification solar distiller unit: An experimental investigation. *Thermal Science and Engineering Progress*, 56, P. 103052. https://doi.org/10.1016/j.tsep.2024.103052.

Abd-ur-Rehman, H.M., Al-Sulaiman, F.A. and Antar, M.A., 2016. Experimental analysis of solar driven multi-stage stepped bubbler humidifier for humidification-dehumidification (HDH) water desalination system. *In Energy Sustainability*, 50220, P. V001T13A002. American Society of Mechanical Engineers. https://doi.org/10.1115/ES2016-59209

Abdelaziz, G.B., Al-Nagdy, A., Kandel, M.G., Dahab, M. and El-Said, E., 2026. Experimental investigation of innovative hybrid solar desalination tower using heat storage and packing materials. *Ren Energy,* 15, P. 125185. https://doi.org/10.1016/j.renene.2026.125185

Ali, A., Sahu, N.K., Khan, M.I., Sharma, P. and Singh, V.R., 2024. Development of a solar device for jute filling based humidification dehumidification desalination. *Australian Journal of Mechanical Engineering*, 22(3), pp. 493-505. https://doi.org/10.1080/14484846.2022.2113618

Alnaimat, F., Ziauddin, M. and Mathew, B., 2025. Humidification and dehumidification desalination utilizing ultrasonic atomization and direct solar energy harvesting. *Desalination* 602, P. 118636. https://doi.org/10.1016/j.desal.2025.118636

Bahramei, R., Samimi-Akhijahani, H., Salami, P. and Behroozi-Khazei, N., 2025. Life cycle assessment and CFD evaluation of an innovative solar desalination system with PCM and geothermal system. *Journal of Energy Storage,* 120, P. 116116. https://doi.org/10.1016/j.est.2025.116116

Cengel, Y.A., 2007. *Heat and mass transfer: a practical approach*. 3rd ed. New York: McGraw-Hill. ISBN-13:978-0073250359

Chen, S., Zhao, P., Xie, G., Wei, Y., Lyu, Y., Zhang, Y., Yan, T. and Zhang, T., 2021. A floating solar still inspired by continuous root water intake. *Desalination* 512, P. 115133. https://doi.org/10.1016/j.desal.2021.115133

Chiranjeevi, C., Srinivas, T. and Shankar, R., 2019. Experimental investigation on a hybrid desalination and cooling unit using humidification-dehumidification technique. *Desalination and Water Treatment*, 156, pp. 148-160. https://doi.org/10.5004/dwt.2019.23680

da Silva Junior, L.G., de Oliveira, J., Ribeiro, G.B. and Ferreira Pinto, L., 2023. Experimental and numerical analysis of a low-cost solar still. *Eng,* 4, pp. 380-403. https://doi.org/10.3390/eng4010023

Duffie, J.A., Beckman, W.A. and Blair, N., 2020. Solar engineering of thermal processes, photovoltaics and wind. John Wiley & Sons.

Dizaji, H.S., Pourhedayat, S., Moria, H., Alqahtani, S., Alshehery, S. and Anqi, A.E., 2023. Performance boost of a commercial air-to-air plate heat recovery unit by mesh-net insert; thermal-frictional, economic, and effectiveness-NTU analysis. *Energy*, 290, P. 130037, https://doi.org/10.1016/j.energy.2023.130037.

Essa, F.A., Mohamed Othman, M., Mohamed Younes, M., Omara, Z.M. and Khalil, H., 2025. Enhancing freshwater production and cost-effectiveness in humidification-dehumidification (HDH) technology: Novel wheat straw packing and configuration optimization. *Energy Sources, Part A: Recovery, Utilization, and Environmental Effects*, 47(1), pp. 11957–11975. https://doi.org/10.1080/15567036.2025.2504541

Guan, B., Liu, X. and Zhang, T., 2021. Exergy analysis on optimal desiccant solution flow rate in heat exchanger for air dehumidification using liquid desiccant. *International Journal of Refrigeration*, 128, pp. 129-138. https://doi.org/10.1016/j.ijrefrig.2021.03.024

Juarez, R.A., Xaman, J., Gabrierla, A.G. and Lopez, I.H., 2015. Numerical study of heat and mass transfer in a solar still device: Effect of the glass cover. *Desalination,* 359, pp. 200-211. https://doi.org/10.1016/j.desal.2014.12.034

Kabeel, A.E., Diab, M.R., Elazab, M.A. and El-Said, E.M.S., 2022. Solar powered hybrid desalination system using a novel evaporative humidification tower: Experimental investigation. *Solar Energy Materials and Solar Cells*, 248, P. 112012. https://doi.org/10.1016/j.solmat.2022.112012

Kaood, A., Abou-Deif, T., Eltahan, H., Yehia, M.A. and Khalil, E.E., 2019. Numerical investigation of heat transfer and friction characteristics for turbulent flow in various corrugated tubes. Proceedings of the Institution of Mechanical Engineers Part A *Journal of Power and Energy*, 233(4). 1 https://doi.org/10.1177/0957650918806407

Kays, W.M., Crawford, M.E. and Weigand, B., 2004. *Convective heat and mass transfer*. 4th ed. McGraw-Hill. ISBN-13: 978-0072468762.

Kline, S.J. and McClintock, F.A., 1953. Describing uncertainties in single sample experiments, *Mech. Eng*. 75, pp. 3–8.

Lafta, A.M. and Amori, K.E., 2022. Field study of absorbent media effect on the yield of solar desalination for Iraqi marsh water. *International Review of Mechanical Engineering*, 16(6), pp. 277-286. https://doi.org/10.15866/ireme.v16i6.22038

Li, Y.J., Yang, Y.Y., Luo, B.G., He, S.B., Liu, C., Chen, Y., Chen, P., Xu, Y.T. and Li, Y.W., 2025. Polyphenolic mechanochemistry-mediated liquid metal hydrogels for efficient solar-powered desalination and electricity generation. *Advanced Functional Materials*, 36(30), P. 28898. https://doi.org/10.1002/adfm.202528898

Mahmoudi, A., Valipour, M.S. and Rashidi, S., 2025. Potentials of porous materials and thermal control system for performance enhancement of humidification-dehumidification desalination unit powered by solar dish collector: Experimental study with 4E analysis. *International Communications in Heat Mass Transfer*, 164, P. 108958. https://doi.org/10.1016/j.icheatmasstransfer.2025.108958

Manesh, M.H.K., Davadgaran, S., Rabeti, S.A.M. and Blanco-Marigorta, A.M., 2024. Optimal 4E evaluation of an innovative solar-wind cogeneration system for sustainable power and fresh water production based on integration of microbial desalination cell, humidification-dehumidification, and reverse osmosis desalination. *Energy*, 297, P. 131256. https://doi.org/10.1016/j.energy.2024.131256

Messaouda, A., Hamdi, M. and Lazaar, M., 2026. Experimental thermal analysis of a clay-based solar desalination system enhanced with phase change material. *Applied Thermal Engineering*, 292, P. 130383. https://doi.org/10.1016/j.applthermaleng.2026.130383

Rahbar, N. and Esfahani, J., 2012a. Productivity estimation of a single-slope solar still: Theoretical and numerical analysis. *Energy,* 49, pp. 289–297. https://doi.org/10.1016/j.energy.2012.10.023

Rahbar, N. and Esfahani, J.A., 2012b. Estimation of convective heat transfer coefficient in a single-slope solar still: a numerical study. *Desalination and Water Treatment,* 50(1–3), pp. 387–396. https://doi.org/10.1080/19443994.2012.720442

Rahimi-Ahar, Z., Hatamipour, M.S. and Ghalavand, Y., 2018. Experimental investigation of a solar vacuum humidification dehumidification (VHDH) desalination system. *Desalination*, 437, pp. 73-80. https://doi.org/10.1016/j.desal.2018.03.002

Rajaseenivasan, T. and Srithar, K., 2016. Potential of a dual purpose solar collector on humidification dehumidification desalination system. *Desalination,* 404, pp. 35–40. https://doi.org/10.1016/j.desal.2016.10.015

Rajaseenivasan, T., Shanmugam, R.K., Hareesh, V.M. and Srithar, K. 2016. Combined probation of bubble column humidification dehumidification desalination system using solar collectors. *Energy,* 116, pp. 459-469. http://dx.doi.org/10.1016/j.energy.2016.09.127

Rastogi, G., 2021. Thermoelectric cooler-supported water condensation system development method. *Ilkogretim Online - Elementary Education Online*, 20, pp. 5205-5212. https://doi.org/10.17051/ilkonline.2021.04.551

Sánchez-Sutil, F., and Cano-Ortega, A., 2021. Performance evaluation and comparative analysis of a DHT22 sensor for applications in Internet of Things. *Sensors* 21(10), P. 3503. https://doi.org/10.3390/s21103503

Shah, R.K. and London, A.L., 1978. *Laminar flow forced convection in ducts. A source book for compact heat exchanger analytical data*. Academic Press, New York, ISSBN-13**:** 978-0-12-020051-1

Shaikh, J.S. and Ismail, S., 2023. Performance evaluation of a solar humidification dehumidification desalination system employing a multistage bubble column dehumidifier. *Solar Energy* 263, P. 111933. https://doi.org/10.1016/j.solener.2023.111933

Tiwari, A. and Kumar, A., 2025. Humidification-dehumidification desalination system based on solar air and water heaters. *Solar Energy* 297, P. 113637. https://doi.org/10.1016/j.solener.2025.113637

Tuğan, V., İnallı, M. and Işık, E., 2025. Experimental analysis of a double-slope solar still integrated with parabolic trough solar collector using nanofluid. *Thermal Science and Engineering Progress* 67, P. 104094. https://doi.org/10.1016/j.tsep.2025.104094

Tourab, A.E., Blanco-Marigorta, A.M., Elharidi, A.M. and Suarez-Lopez, M.J., 2023. A novel configuration of hybrid reverse osmosis, humidification–dehumidification, and solar photovoltaic systems: modeling and exergy analysis. *Journal of Marine Science Engineering*, 12 (1), P. 19. https://doi.org/10.3390/jmse12010019

Wang, B., Shen, J., Zhu, W. and Wang, W., 2024. Analysis of heat pump operated two-stage humidification- dehumidification desalination system with subcooler and heat regenerator. *Desalination*, 581, P. 117593. https://doi.org/10.1016/j.desal.2024.117593

Wang, D.Y., Bu, Y.M., Wu, X., Owens, G. and Xu, H.L., 2026. A 3D printed cu evaporator support for record-high interfacial solar evaporation. Material Horizons. https://doi.org/10.1039/d5mh02102b

Welepe, H.J., Gunerhan, H. and Bilir, L., 2022. Humidifying solar collector for improving the performance of direct solar desalination systems: A theoretical approach. *Applied Thermal Eng*., 216, P. 119043. https://doi.org/10.1016/j.applthermaleng.2022.119043

Wu, P., Wu, X., Wang, Y., Xu, H. and Owens, G., 2022. A biomimetic interfacial solar evaporator for heavy metal soil remediation. *Chemical Engineering Journal*, 435 P. 143793. https://doi.org/10.1016/j.cej.2022.134793

Zhang, C.H., Yan, Y., Wu, Y.H., Liu, C., Huang, J., Hu, Y., Li, Y. and Yang, Z.Q., 2026. Phase-change-integrated magnetic porous carbon for synergistic magnetothermal and photothermal interfacial evaporation. *Energy Conversion and Management*, 349, P. 120813. https://doi.org/10.1016/j.enconman.2025.120813

Ziauddin, M., Alnaimat, F. and Mathew, B., 2025. Solar humidification and dehumidification system: Integrating ultrasonic atomizer and solar still state-of-art. *Sep. Purif. Technol*. 378, P. 134550. https://doi.org/10.1016/j.seppur.2025.134550

Zubair, S.M. and Antar, M.A., Elmutasim, S.M., Lawal D.U., 2018. Performance evaluation of humidification-dehumidification (HDH) desalination systems with and without heat recovery options: an experimental and theoretical investigation. *Desalination* 436, pp. 161–175. https://doi.org/10.1016/j.desal.2018.02.018

التقييم العملي لتبخر الماء بالتنقيط في منظومة مُرطِّب شمسي باستخدام لوح ماص مستوي ومنقّر

سعد محسن الساعدي، كريمة اسماعيل عموري*

قسم الهندسة الميكانيكية، كلية الهندسة، جامعة بغداد، بغداد، العراق

الخلاصة

تُعدّ تحلية المياه قليلة الملوحة ومياه البحر باستخدام مصادر الطاقة المتجددة استراتيجية فعّالة لتوفير مياه الشرب. يركّز هذا البحث على تطوير منظومة ترطيب شمسية كهربائية–حرارية منخفضة الكلفة ومنخفضة الدرجة الحرارية، والتي تُعدّ حلاً واعدًا وبسيطًا لإنتاج المياه العذبة على النطاق الصغير. وقد تم تصميم وتجهيز مُرطِّب شمسي يستثمر الإشعاع الشمسي بصورة مباشرة، مع تزويده بتيار هواء ساخن قسري لزيادة كفاءة تبخير قطرات الماء الساخن الساقطة على سطح ممتص نحاسي مطلي باللون الأسود .يتم تسخين كلٍّ من الماء والهواء مسبقًا بواسطة مجمّع شمسي مسطّح ومجمّع هواء شمسي، على التوالي، قبل دخولهما إلى المُرطِّب. وشملت العوامل الرئيسة المؤثرة في الرطوبة النسبية للهواء: معدلات تدفق الهواء (من 0.5 إلى 1.5 م³/دقيقة)، ومعدل تقاطر الماء (من 5 إلى 10 قطرات/ثانية)، إضافةً إلى هندسة سطح الماصّات الحرارية (المسطح أو المنقّر) داخل المُرطِّب الشمسي. أُجريت الاختبارات خلال الفترة من الساعة 8:00 صباحًا حتى 5:00 مساءً لتقييم الرطوبة النسبية ودرجة حرارة الهواء في الأيام الصافية بمدينة بغداد، العراق، خلال شهر تشرين الأول/أكتوبر 2025. أظهرت النتائج أن أعلى رطوبة نسبية للهواء عند مخرج المُرطِّب بلغت 61.2% و72.4% و69.9% عند معدلات تقاطر ماء مقدارها 4 و7 و10 قطرات/ثانية على التوالي، مع تثبيت معدل تدفق الهواء عند 0.5 م³/دقيقة. كما تبيّن أن أفضل معدل للتقاطر هو 7 قطرات/ثانية عند معدل تدفق هواء مقداره 0.5 م³/دقيقة. بلغت الرطوبة النسبية للهواء الخارج من المُرطِّب 72.4% و85.6% عند استخدام الماصّ المسطح والماصّ المنقّر على التوالي، وذلك عند معدل تدفق هواء مقداره 0.5 م³/دقيقة ومعدل تقاطر 7 قطرات/ثانية. كما بلغت كفاءة المُرطِّب 70% و85% على التوالي. ويُستنتج من ذلك أن سطح اللوح الماصّ المنقّر يحقق أداءً أفضل بصورة ملحوظة في عملية الترطيب مقارنةً بالسطح المسطح، وذلك تحت جميع معدلات تدفق الهواء التي تم اختبارها.

الكلمات المفتاحية :المرطب الشمسي، السطح الماص المحقّر، المجمع الشمسي، التبخر، القطرات.